We are IntechOpen, the world's leading publisher of Open Access books
Built by scientists, for scientists

6,900
Open access books available

186,000
International authors and editors

200M
Downloads

154
Countries delivered to

Our authors are among the

TOP 1%
most cited scientists

12.2%
Contributors from top 500 universities

WEB OF SCIENCE™

Selection of our books indexed in the Book Citation Index
in Web of Science™ Core Collection (BKCI)

Interested in publishing with us?
Contact book.department@intechopen.com

Numbers displayed above are based on latest data collected.
For more information visit www.intechopen.com

The Mechanical Behavior of the Cable-in-Conduit Conductor in the ITER Project

Donghua Yue, Xingyi Zhang and Youhe Zhou

Abstract

Cable-in-conduit conductor (CICC) has wide applications, and this structure is often served to undergo heat force-electromagnetic coupled field in practical utilization, especially in the magnetic confinement fusion (e.g., Tokamak). The mechanical behavior in CICC is of relevance to understanding the mechanical response and cannot be ignored for assessing the safety of these superconducting structures. In this chapter, several mechanical models were established to analyze the mechanical behavior of the CICC in Tokamak device, and the key mechanical problems such as the equivalent mechanical parameters of the superconducting cable, the untwisting behavior in the process of insertion, the buckling behavior of the superconducting wire under the action of the thermo-electromagnetic static load, and the Tcs (current sharing temperature) degradation under the thermo-electromagnetic cyclic loads are studied. Finally, we summarize the existing problems and the future research points on the basis of the previous research results, which will help the related researchers to figure out the mechanical behavior of CICC more easily.

Keywords: Nb3Sn, cable in conduit conductor (CICC), cable stiffness, coefficient of thermal expansion, untwisting, current sharing temperature

1. Introduction

The ITER program is one of the largest and the most influential international energy technology cooperation projects, to verify the engineering feasibility of the magnetic confinement fusion. The core device of the magnetic confinement fusion reactor is the cable-in-conduit conductor (CICC). CICCs were used to build up the superconducting coil for generating strong magnetic fields to confine the high-temperature plasma in a confined space and maintaining the fusion reaction [1]. The ITER superconducting magnet systems mainly consist of four kinds of coils: 6 central solenoids (CS), 18 toroidal field (TF) coils, 6 sets of poloidal field (PF) coils, and 9 pairs of correction fields coils (CC) [2].

As early as the 1960s, the low-temperature superconducting material NbZr was processed into round wire and cables [3]. Subsequently, the superconducting magnets were wound with the structure of an internally cooled conductor (ICS) [4]. The superconducting strand is cooled to the superconducting state by the heat transfer copper tube with liquid helium in it [5]. But, the contact cooling method of ICS is inefficient, and the superconducting material is inclined to have a magnetic

flux jump which will make the magnetic system to be quenched. In 1975, Hoenig et al. suggested subdividing the superconductor into strands to suppress the flux jump and twisting them into a cable to reduce the AC losses [6]. In 1980, Lue et al. proposed a cable-in-conduit design, and the innermost part was a perforated copper tube or a high-hardness stainless steel spring to form a liquid helium fast-flowing channel [7]. These two designs are the prototypes of modern CICC conductors. Nowadays, the CS and TF conductors with higher magnetic fields in the ITER project were fabricated by more than 1000 Nb3Sn wires. Disadvantageously, the superconducting properties of Nb3Sn are sensitive to mechanical deformation, which means that the tensile, compressive, and torsional deformations all lead to the reduction of the critical current [8]. Therefore, the strain state of the Nb3Sn strand cannot be ignored. Therefore, during its design, manufacture, and operation stage of the CICC, the mechanical analysis is needed.

Many studies have been published on the equivalent mechanical parameters of the twisted cable with two dimensions, such as the compression modulus of the cross section [9, 10], rather than built a complete three-dimensional model of the twisted cable. Feng et al. have applied the thin rod model to CICC conductor analysis and established the spatial geometry of each superconducting strand in the CICC conductor [11]. Qin et al. have applied the thin rod model to the mechanical analysis of superconducting cables and derived the axial stress–strain curves of primary cables and high-order strands [12]. The influence of pitch on the elastic modulus of the stranded cable and the curvature of the strand has been discussed. The introduction of the copper strand has been found to greatly reduce the axial stiffness of the strand, and the contact deformation between the strands has been found to have a great influence on the stiffness of the strand. The theoretical calculation results have appeared to be in good agreement with the experiments [13, 14]. Yue et al. have conducted a systematic mechanical analysis of the CICC in the design, preparation, and operation stage [15–18].

In this chapter, first of all, we focus on the equivalent mechanical parameters of the superconducting cable; second, we concentrate on the untwisting behavior in the process of insertion; third, we want to explain the buckling behavior of the superconducting wire under the action of the thermo-electromagnetic static load; and finally, the Tcs degradation under the thermo-electromagnetic cyclic loads is studied. Our goal is to relate the cable stresses and buckling behavior to the thermal and electromagnetic loads so that relations between cable stress and current transport characteristics are built completely.

2. The equivalent mechanical parameters of the CICC

The mechanical behaviors of CICC have two main problems of structure and operation. On the one hand, the equivalent modulus of the cable is dependent on the manufacture parameters such as pitch, porosity, and radius. On the other hand, the electromagnetic load and the extremely low temperature make the internal stress and strain state of the cable difficult to analyze. Therefore, the thin rod model is applied to calculate the equivalent mechanical parameters of CICC conductors.

2.1 The tensile stiffness of the triplet

From the geometry characteristics of the cable, we know that the CICC superconducting cables have a complex structure with five stages of spirals.
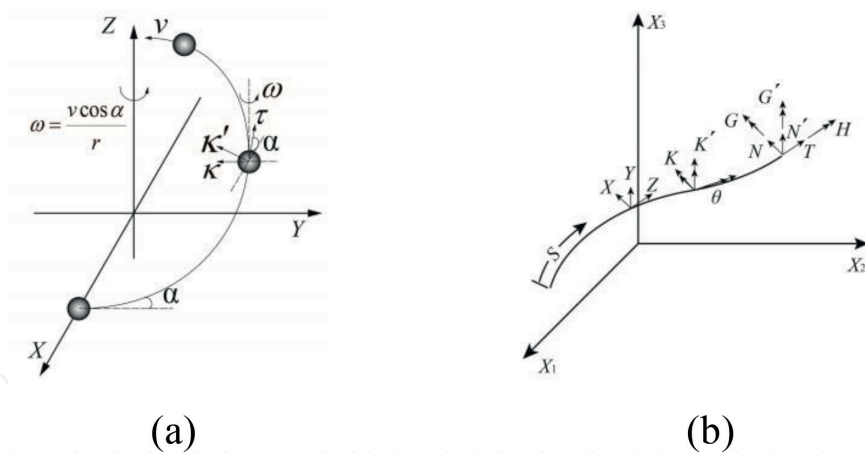
Figure 1.
The position of a spiral rod (a) and loads acting on the wire (b) [19].

Therefore, each wire in the cable can be simplified into a thin rod which is elongated in the axial direction under the axial tensile load, and the wires can be contacted tightly or rotate in the lateral direction. The deformation and the force analysis of the wires are shown in **Figure 1(a)** and **(b)**, respectively.

The curvature and torsion of the spiral are as follows:

$$\kappa = 0; \kappa' = \frac{vdt \cos^2\alpha}{rds} = \frac{\cos^2\alpha}{r}; \tau = \frac{vdt \cos\alpha \sin\alpha}{rds} = \frac{\cos\alpha \sin\alpha}{r}. \tag{1}$$

The equilibrium equation of forces and moments can be expressed as

$$\frac{dN}{ds} + T\kappa' - N'\tau + X = 0; \qquad \frac{dG}{ds} - G'\tau + Hk' - N' + K = 0;$$

$$\frac{dN'}{ds} - Tk + N\tau + Y = 0; \qquad \frac{dG'}{ds} - Hk + G\tau + N + K' = 0; \tag{2}$$

$$\frac{dT}{ds} - Nk' + N'k + Z = 0; \qquad \frac{dH}{ds} - Gk' + G'k + \Theta = 0.$$

Assuming that the thin rod is isotropic and elastic, the moments in any cross section with respect to the axis x, y, z can be written as I_x, I_y, I_z, and the constitutive equations are given by

$$G = EI_x\Delta\kappa; G' = EI_y\Delta\kappa'; H = GI_z\Delta\tau. \tag{3}$$

In the result of solving Eq. (3) with the account for the temperature terms, the expression of the equivalent coefficient of thermal expansion in the axial direction of the triplet can also be given by [15]

$$\alpha_{\text{eff}} = \frac{\alpha_L - \alpha_T \cos^2\alpha}{\sin^2\alpha}. \tag{4}$$

In Eq. (4), α_{eff} is the equivalent coefficient of thermal expansion of the strand, α_L is the coefficient of thermal expansion of the strand in the longitudinal direction, α_T is the transverse coefficient of thermal expansion of the strand, and α denotes the helix angle.

2.2 The tensile stiffness of the higher stage strand

Based on the equivalent modulus and thermal expansion of the triplet, the space and the 2D view of the triplet and single wire are shown in **Figure 2(a)** and **(b)**, respectively.

The conversion relationship between the local coordinates of the triplet and the higher-level strand can be expressed as

$$
T_k = \begin{bmatrix} -\cos\theta_k & -\sin\theta_k & 0 \\ \sin\theta_k \sin\alpha_k & -\cos\theta_k \sin\alpha_k & \cos\alpha_k \\ -\sin\theta_k \cos\alpha_k & \cos\theta_k \cos\alpha_k & \sin\alpha_k \end{bmatrix}.
\tag{5}
$$

The curvature and torsion of the secondary stage strand can be given by

$$
\begin{bmatrix} \kappa_{p2} \\ \kappa_{b2} \\ \kappa_{t2} \end{bmatrix} = T_2 T_1 \left\{ T_1^T \begin{bmatrix} 0 \\ 0 \\ \dfrac{\cos\alpha_2}{r_2} \end{bmatrix} + \begin{bmatrix} 0 \\ 0 \\ \dfrac{\cos\alpha_1}{r_1} \end{bmatrix} \sin\alpha_2 \right\}.
\tag{6}
$$

According to the geometric compatibility of the secondary-stage strand, the deformation of the triplet is equal to the tangential strain of the secondary-stage strand, and the torsion of the triplet is equal to the twist angle of the secondary cable. The axial loads and torque of the secondary-stage strand can be obtained. The equilibrium equations can be expressed as

$$
\begin{bmatrix} 0 \\ 0 \\ F_{t0} \end{bmatrix} = 3{*}3{*}T_1 T_2 \begin{bmatrix} F_{p2} \\ F_{b2} \\ F_{t2} \end{bmatrix}
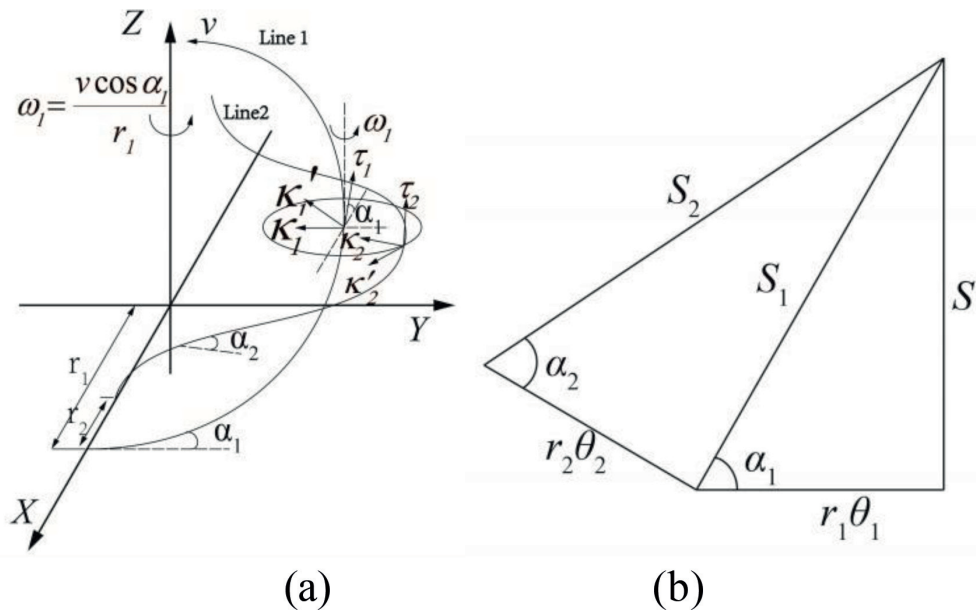\tag{7}
$$

(a)　　　　　　　　(b)

Figure 2.
Space line of the triplet and single wire (a) and 2D view of the triplet and single wire (b).

$$
\begin{bmatrix} M_{p1} \\ M_{b1} \\ M_{t1} \end{bmatrix} = 3T_2 \begin{bmatrix} M_{p2} \\ M_{b2} \\ M_{t2} \end{bmatrix} + 3 \begin{bmatrix} r_2(F_{t2}\sin\alpha_2 + F_{b2}\cos\alpha_2)\sin\theta_2 \\ -r_2(F_{t2}\sin\alpha_2 + F_{b2}\cos\alpha_2)\cos\theta_2 \\ r_2(F_{t2}\cos\alpha_2 - F_{b2}\sin\alpha_2) \end{bmatrix}. \tag{8}
$$

Theoretically, the tensile stiffness of the conductor can be deduced by four times transformations as the CICC conductor has a five-stage twist structure.

3. Rotation analysis of the CICC

In the CICC conductor manufacture process, they twist a superconducting cable and penetrate it into the stainless steel tube. However, due to the friction between the superconducting cable and the stainless steel armor, the drag force of the cable is as high as several tons during the cable penetration. The friction force of the pipe leads to the axial elongation of the superconducting cable, accompanied by the untwisting of the cable, which causes the cable pitch to increase. This makes that the pitch is much larger than the ITER requirement [20]. Therefore, the untwist behavior of the cable must be controlled [17].

In this section, the untwist model is described. The large-scale cable is considered, e.g., ITER TF, CS, and CFETR CSMC. The components of the final cable include petals, central cooling spiral, and wrap, as shown in **Figure 3**. The model ignores the friction between the jacket and the cable, only modeling de-twists of the cable under the insertion force F_{Insert}.

The cable is divided into three parts in the model: central cooling spiral, six petals, and the wrap. The twist direction of wrap and cooling spiral is left and with the reverse direction for the petal. The torsion constraint is free for the cable when there is undering the uniaxial tension. Therefore, the boundary conditions can be set as $F = F_0; M = 0$. The force of the whole cable is from those acts on wrap, sub-cables, and central cooling spiral, which can be described as follows:

$$
\begin{aligned}
F &= F_{in} + F_p + F_{st} = F_0, \\
M &= M_{in} + M_p + M_{st} = 0.
\end{aligned} \tag{9}
$$

In Eq. (9), F is the insertion force in the axial direction for the cable. F_{st}, F_p, F_{in} are the forces loading on the stainless steel wrap, petals, and inner cooling spiral,
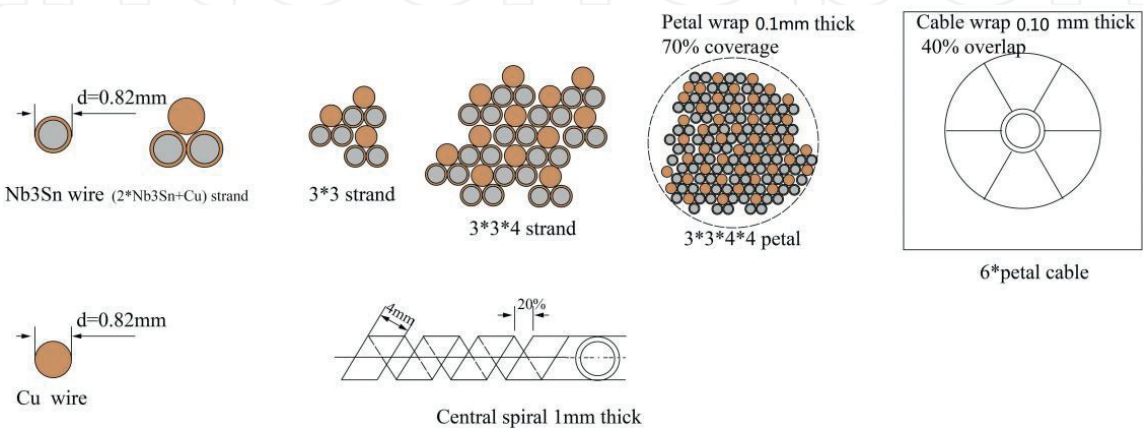

Figure 3.
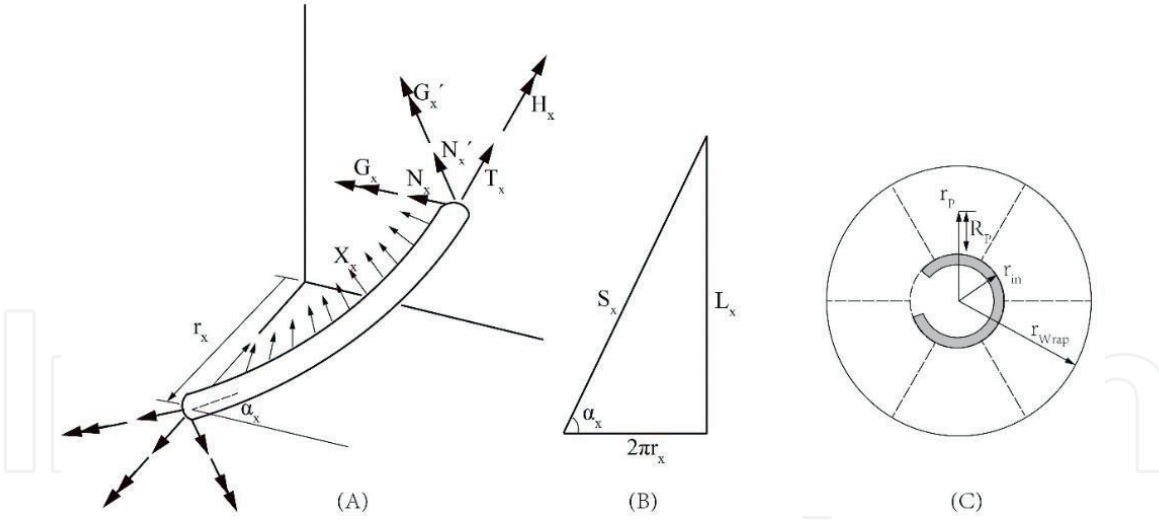*The dimensions and parameters of a large-scale cable (e.g., CFETR CSMC).*

Figure 4.
Force distribution (A) and spatial relationship (B and C).

respectively; M represents the torque of the whole cable. M_{st}, M_p, M_{in} denote the torques of stainless steel wrap, petals, and inner cooling spiral.

The force distribution and spatial relationship are shown in **Figure 4**. G_x, G_x', H_x are sectional moment components of the thin rod. N_x, N_x', T_x are the sectional force components. X_x is the contact force. α_x is the spiral angle of each component. r_x is the distance between the centroid and the center of the cable, and L_x is the twist pitch.

We simplified the central cooling spiral into a single helical thin plate. The change of spiral angle, radius, and the axial strain are defined as $\Delta\alpha_{st}$, $\frac{\Delta r_{st}}{r_{st}}$, ξ_{st}, respectively. Then, the geometrical equations of the He-inlet spiral, six petals, and stainless steel wrap can be deduced by Costello-Velinsky theory [19]; we can obtain

$$He - inlet : \begin{cases} \varepsilon_0 = \xi_{in} + \dfrac{\Delta\alpha_{in}}{\tan\alpha_{in}}, \\[2ex] \beta_0 = \dfrac{\xi_{in}}{\tan\alpha_{in}} + \dfrac{1}{\tan\alpha_{in}}\dfrac{\Delta r_{in}}{r_{in}} - \Delta\alpha_{in}, \end{cases}$$

$$Petal : \begin{cases} \varepsilon_0 = \xi_P + \dfrac{\Delta\alpha_P}{\tan\alpha_P}, \\[2ex] \beta_0 = \dfrac{\xi_P}{\tan\alpha_P} + \dfrac{1}{\tan\alpha_P}\dfrac{\Delta r_P}{r_P} - \Delta\alpha_P, \end{cases} \tag{10}$$

$$Wrap - stiffness : \begin{cases} \varepsilon_0 = \xi_{st} + \dfrac{\Delta\alpha_{st}}{\tan\alpha_{st}}, \\[2ex] \beta_0 = \dfrac{\xi_{st}}{\tan\alpha_{st}} + \dfrac{1}{\tan\alpha_{st}}\dfrac{\Delta r_{st}}{r_{st}} - \Delta\alpha_{st}. \end{cases}$$

In the equations, the axial deformation and torsion angle of the cable are expressed as ε_0, β_0. The only axial tension is considered for central cooling spiral and wrap. Therefore, the equations can be updated as

$$He - inlet : \begin{cases} G_{in} = 0; G'_{in} = 0; H_{in} = 0 \\ \\ T_{in} = E_{in}A_{in}\xi_{in} \end{cases}$$

$$Petal : \begin{cases} G_P = 0; G'_P = E_P I^x_P \Delta\kappa'_P; H_P = G_P I^z_P \Delta\tau_P \\ \\ T_P = E_P A_P \xi_P \end{cases} \quad (11)$$

$$Wrap - stiffness : \begin{cases} G_{st} = 0; G'_{st} = 0; H_{st} = 0 \\ \\ T_{st} = E_{st}A_{st}\xi_{st} \end{cases}$$

In the equation systems, E refers to Young's modulus of each component. A refers to the cross section of each component. $E_P I^x_P$, $G_P I_P$ are the bending and torsion stiffness of petals, respectively. $\Delta\kappa'_P$, $\Delta\tau_P$ are the changes in curvature and twist, respectively. ξ_P is the axial strain of petal.

The balance equations and the compatible equations of central cooling spiral, subcables, and wrap can be obtained as

$$N'_x = G'_x \tau_x + H_x \kappa'_x,$$

$$X_x = N'_x \tau_x - T_x \kappa'_x,$$

$$(12)$$

$$F_x = T_x \sin\alpha_x + N'_x \cos\alpha_x,$$

$$M_x = H_x \sin\alpha_x + G'_x \cos\alpha_x + T_x r_x \cos\alpha_x - N'_x r_x \sin\alpha_x.$$

$$r_{in} = R_{in}; r_P = R_{in} + R_P; r_{st} = R_{in} + 2R_P,$$

$$(13)$$

$$\Delta r_{in} = \Delta R_{in}; \Delta r_P = \Delta R_{in} + \Delta R_P; \Delta r_{st} = \Delta R_{in} + 2\Delta R_P.$$

where x stands for anyone of in, p, st, which represent inner He-inlet spiral, petal, and stainless steel wrap, respectively; R_p denote the twist radius of petal, and $\Delta R_P = -\nu R_P \xi_P$, ν is Poisson's ratio of the petal.

The contact force loading on the petal can be written as follows:

$$\frac{6X_P}{\sin\alpha_P} = \frac{X_{st}}{\sin\alpha_{st}} - \frac{X_{in}}{\sin\alpha_{in}} \quad (14)$$

where X_P stand for the line pressure between the petal and inner He-inlet spiral; X_{st} is the uniform force between the stainless steel wrap and petal; and X_{in} is the reaction force between inner He-inlet spiral and petal.

From Eqs. (9)–(12), one can get

$$F = F_0 = 6(T_P \sin\alpha_P + N'_P \cos\alpha_P) + T_{st} \sin\alpha_{st} + T_{in} \sin\alpha_{in}$$

$$M = 0 = 6(H_P \sin\alpha_P + G'_P \cos\alpha_P + T_P r_P \cos\alpha_P - N'_P r_P \sin\alpha_P) \quad (15)$$

$$-T_{st} r_{st} \cos\alpha_{st} - T_{in} r_{in} \cos\alpha_{in}$$

From the above Eqs. (10)–(15), we can obtain

$$\left(\frac{1}{\tan \alpha_{st}} + \tan \alpha_p\right)\xi_{st} - \frac{vr_p}{\tan \alpha_{st}}\frac{2}{r_{in} + 2R_P}\xi_P + 0 \cdot \xi_{in} + \frac{1}{\tan \alpha_{st}}\frac{1}{r_{in} + 2R_P}\Delta r_{in} - \tan \alpha_{st}\varepsilon_0 - \beta_0 = 0$$

$$0 \cdot \xi_{st} + \left(\frac{1}{\tan \alpha_p} + \tan \alpha_p - \frac{vR_P}{\tan \alpha_P}\frac{1}{r_{in} + R_P}\right)\xi_P + 0 \cdot \xi_{in} + \frac{1}{\tan \alpha_P}\frac{1}{r_{in} + R_P}\Delta r_{in} - \tan \alpha_P\varepsilon_0 - \beta_0 = 0$$

$$0 \cdot \xi_{st} + 0 \cdot \xi_P + \left(\tan \alpha_{in} + \frac{1}{\tan \alpha_{in}}\right)\xi_{in} + \frac{1}{r_{in}\tan \alpha_{in}}\Delta r_{in} - \tan \alpha_{in}\varepsilon_0 - \beta_0 = 0$$

$$-\frac{\sin \alpha_P}{6\sin \alpha_{st}}(EA)_{st}\kappa'_{st}\xi_{st} + \left[GB\tau_P + HB\kappa'_P - (EA)_P\kappa'_P\right]\xi_P + \frac{\sin \alpha_P}{6\sin \alpha_{in}}(EA)_{in}\kappa'_{in}\xi_{in} + (GD\tau_P + HD\kappa'_P)\Delta r_{in}$$

$$+ (GE\tau_P + HE\kappa'_P)\varepsilon_0 + 0 \cdot \beta_0 = 0$$

$$(EA)_{st}\sin \alpha_{st}\xi_{st} + \left[6GB\tau_P\cos \alpha_P + 6HB\kappa'_P\cos \alpha_P + 6(EA)_P\sin \alpha_P\right]\xi_P + (EA)_{in}\sin \alpha_{in}\xi_{in}$$

$$+ 6(GD\tau_P + HD\kappa'_P)\cos \alpha_P\Delta r_{in} + 6(GE\tau_P + HE\kappa'_P)\cos \alpha_P\varepsilon_0 + 0 \cdot \beta_0 = F_0$$

$$- (EA)_{st}\cos \alpha_{st}r_{st}\xi_{st} + \left[6HB\sin \alpha_P + 6GB\cos \alpha_P + 6(EA)_P(r_{in} + r_P)\cos \alpha_P - 6(GB\tau_P + HB\kappa'_P)r_P\sin \alpha_P\right]\xi_P$$

$$- (EA)_{in}\cos \alpha_{in}r_{in}\xi_{in} + \left[6HD\sin \alpha_P + 6GD\cos \alpha_P - 6(GD\tau_P + HD\kappa'_P)r_P\sin \alpha_P\right]\Delta r_{in}$$

$$+ \left[6HE\sin \alpha_P + 6GE\cos \alpha_P - 6(GE\tau_P + HE\kappa'_P)r_P\sin \alpha_P\right]\varepsilon_0 + 0 \cdot \beta_0 = M_0$$

$$(16)$$

The twist angle β_0 can be computed from the equation system (16). So, the rotation of cable can be evaluated [17].

The experimental and numerical results are shown in **Figure 5**. First, it is easily found that the cabling tension has less impact on cable rotation. Taking the wrapping tension with 200 N, for example, there is no deviation between two different cables with cabling tension 200 N and 800 N, respectively. This result is in good agreement with the numerical model results. Second, the untwisting of the cable was mainly controlled by wrapping tension. Therefore, we can reduce the rotation significantly by increasing the wrapping tension. When insertion force is about 40 kN, the untwisting angle of cables with 600 N wrapping tension is about half of those cases with 200 N.
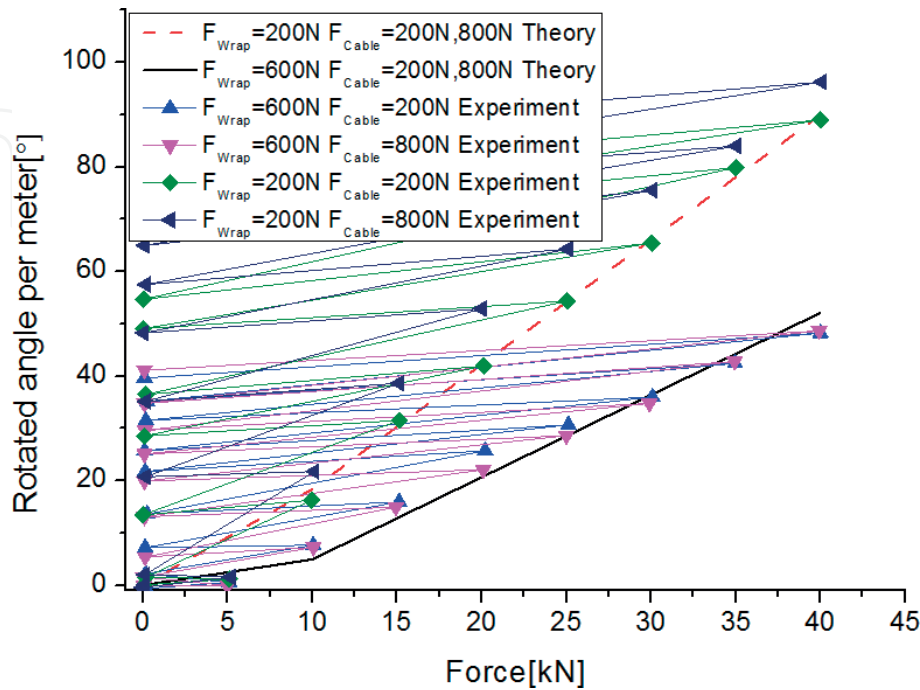

Figure 5.
Rotated angle per meter as a function of the force: Numerical and experimental results.

4. Buckling behavior in the CICC

4.1 Analytical model without the electromagnetic force

It is known that all the ITER CS and TF coils are wounded by CICCs, which made up of five-stage sub-cables formed around a central cooling tube. The petals and the sub-cables are wrapped with stainless steel tapes. Then, let the wrapped cable inserted into a stainless steel tube, which act as an amor. We assume that the total length of free segment of the superconducting strand on the surface of the cable is L (equal to the twist pitch), and set the fixed constraints on both sides, the wrap band as a uniform spring constraint. The schematic of this analytical model is illustrated in **Figure 6**. The lengths of spring constraint on both sides are equal to L_1 and L_3, respectively. The length of the free fraction of the strand is of L_2; we can get $L_1 + L_2 + L_3 = L$.

Since the coefficient of thermal expansion of stainless steel between 923 and 4.2 K is approximately twice that of the Nb3Sn strand, then the superconducting cable is in compression at the end of the cooling. The thermal shrinkage of the cable is denoted by $\varepsilon_{Thermal}$. Other than this, the strands of the cable can be squeezed into another side of the conduit by the large electromagnetic force; then, there will generate a large void on the other side of the conduit. Due to the gap, the friction force between the strands and the stainless steel armor decrease significantly. As there is no lateral restraint by wrap or friction, the surface strands around the void will show bending deformation by the thermal mismatch. In addition, the strand will slide into the high magnetic field region that will aggravate its bending behavior. ε_{Slid} is the stand for this slid strain. Therefore, the total compression strain of the strand ε_T is the sum of ε_{Slid} and $\varepsilon_{Thermal}$. In this case, $\varepsilon_T = \varepsilon_{Thermal} + \varepsilon_{Slid}$.

The mechanical analysis of the strand microelement is shown in **Figure 7**. The equilibrium equations for the moments are as follows:

$$\frac{dM}{dx} + N\frac{dy}{dx} - Q_v = 0 \tag{17}$$

In Eq. (17), Q_v, M, N denote the vertical shear force, the bending moment, and the compression force along the axial direction, respectively. After submitting $M = -EI(d^2y/dx^2)$ into Eq. (17), and making a substitution $dQ_v/dx = ky$, we can get the differential equation of the rod with the spring constraints:

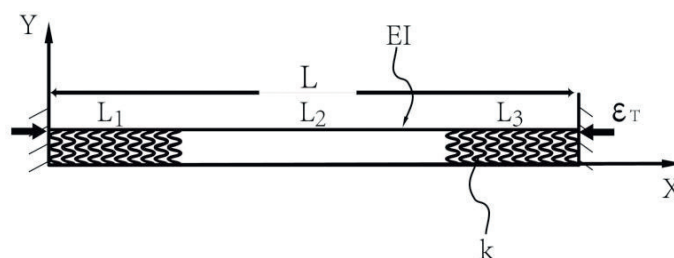$$EI\frac{d^4y}{dx^4} - N\frac{d^2y}{dx^2} + ky = 0 \tag{18}$$

Figure 6.
Schematic of the strand model ignores the EM force. L, L_1, L_2 and L_3 denote the length of the twist pitch, left spring constraint, free segment, and right spring constraint, respectively. k denotes the rigidity of the bandaging. EI is the bending stiffness of the strand. ε_T is the total compression strain, which is equal to the sum of $\varepsilon_{Thermal}$ and ε_{Slid}.
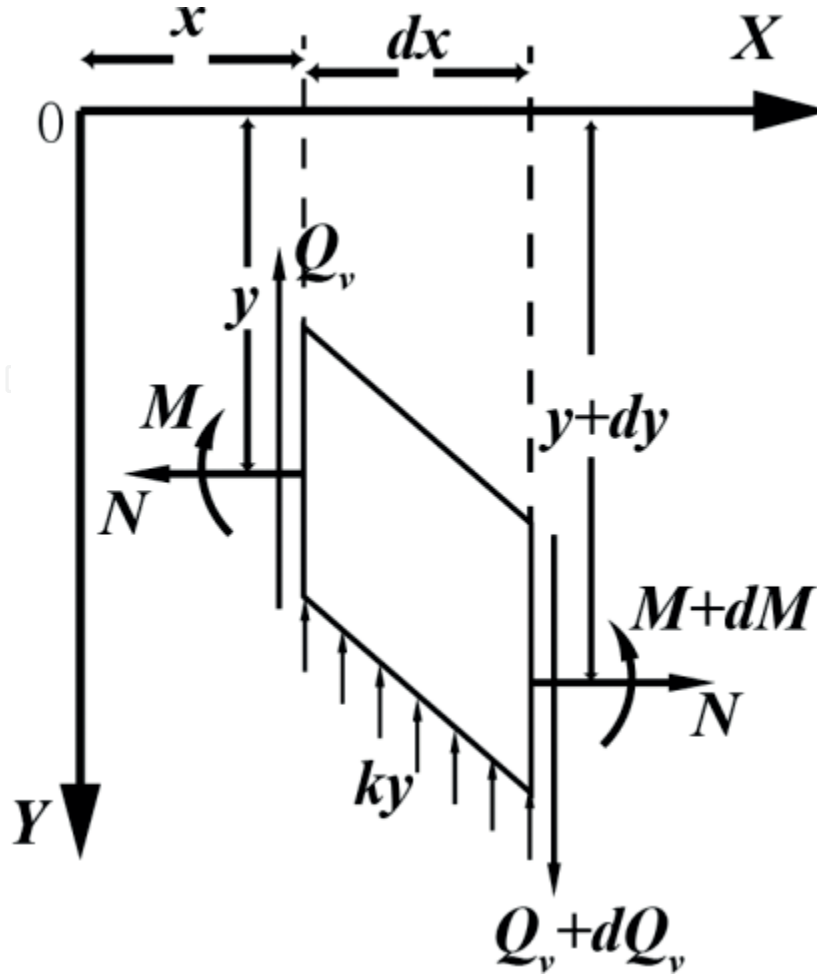
Figure 7.
Mechanical analysis for the strand microelement.

If the strand has no wrapping, one can get

$$EI\frac{d^4y}{dx^4} - N\frac{d^2y}{dx^2} = 0 \tag{19}$$

where k denotes the stiffness of the wrapping.

The continuity of displacements, twist angles, bending moments, and shear forces across the coverage/free strand require

$$
\begin{aligned}
w_i &= w_{i+1} \\
\frac{dw_i}{dx_i} &= \frac{dw_{i+1}}{dx_{i+1}} \\
\frac{d^2w_i}{dx_i^2} &= \frac{d^2w_{i+1}}{dx_{i+1}^2} \\
-\left[N\frac{dw_i}{dx_i} + \frac{d^3w_i}{dx_{i+1}^3}\right] &= -\left[N\frac{dw_{i+1}}{dx_{i+1}} + \frac{d^3w_{i+1}}{dx_{i+1}^3}\right]
\end{aligned}
\tag{20}
$$

In Eq. (20) the subscript i represents the number of wrapping/free segments. The fixed boundary conditions at the coverage fraction have the form:

$$w|_{x=0} = w|_{x=L} = 0$$

$$\frac{dw}{dx}\bigg|_{x=0} = \frac{dw}{dx}\bigg|_{x=L} = 0 \tag{21}$$

Thus, the general solution of Eq. (18) is obtained as

$$w_i = a_{i1}\cos(\lambda x_i) + a_{i2}\sin(\lambda x_i) + a_{i3}x_i + a_{i4} \tag{22}$$

This general solution can be divided into three situations with a variation of the external force P [21–23]:

1. If $P \leq 2\sqrt{EIk}$, the general solution has the form as

$$w_i = a_{i1}\cosh(\lambda_1 x_i) + a_{i2}\cosh(\lambda_2 x_i) + a_{i3}\sinh(\lambda_1 x_i) + a_{i4}\sinh(\lambda_2 x_i) \tag{23}$$

2. If $P = 2\sqrt{EIk}$, it becomes

$$w_i = a_{i1}\cos(\lambda x_i) + a_{i2}\cos(\lambda x_i) + a_{i3}x_i\sin(\lambda x_i) + a_{i4}x_i\sin(\lambda x_i) \tag{24}$$

3. If $P \geq 2\sqrt{EIk}$, it becomes

$$w_i = a_{i1}\cos(\lambda_1 x_i) + a_{i2}\cos(\lambda_2 x_i) + a_{i3}\sin(\lambda_1 x_i) + a_{i4}\sin(\lambda_2 x_i) \tag{25}$$

Here, λ, λ_1, λ_2 and λ_3 are the eigenvalues, respectively; and a_{ij} is the constant coefficients.

The axial compression strain can be neglected when the strand gets into the buckling state, as the compression force N is small. Therefore, the total compression of the strand can be expressed as

$$\frac{1}{2}\int_0^L (w')^2 dx = L\varepsilon_T - \frac{NL}{EA} \tag{26}$$

Here, w' denotes the curvature of the strand transverse deflection. The radius of curvature ρ has the form

$$\rho = \frac{d^2 w}{d^2 x} \tag{27}$$

Here, w stands for the strand transverse deflection. The corresponding maximum strain is

$$\varepsilon_{\max} = \frac{D}{2\rho} \tag{28}$$

Here, D stands for the diameter of the strand. If the maximum strain is larger than 1%, the strand would be considered as cracking [10, 24–26]. Based on these equations, the coefficient a_{ij} can be calculated, as well as the buckling deflection, the

relationship between the radius of curvature, and the thermal compression strain $\varepsilon_{Thermal}$ or slid strain ε_{Slid}.

4.2 Analytical model with the electromagnetic force

As we know, the magnetic field is maintained at 13 T in the Tcs test procedure, and the electromagnetic force rises with the increasing the current. Therefore, the electromagnetic force is a cyclic load. The strand on the surface of the cable where the gap is formed is selected in this model. The EM force F_{EM} is perpendicular to the Nb3Sn strand, and its direction points to the inner part of the cable. Thus, the strand at the lower loading side has the least lateral constraint that means the strand most likely to have a buckling behavior in the lateral direction. Therefore, the only thing that can prevent the buckling of the strands is the friction force against the cable. The friction factor can be written as a symbol μ.

In **Figure 8**, μ_L and μ_T are the axial friction factor and lateral friction factor, respectively; L_s and L denote the slipping length and buckling length, respectively; $L + 2L_s$ is the twist pitch of the first stage; F_{EM} stands for the EM force, and then in the buckling area $\mu_T F_{EM}$ is the lateral constraint on the strand; and P_0 and P are the compression force of the strand in the slipping and buckling area, respectively.

Accordingly, by the torque balance of the microelement, as shown in **Figure 9**. The equilibrium equation is as follows:

$$-EIy'' = Py + \frac{\mu_T F_{EM}}{2}\left(\frac{L}{2} - x\right)\left(\frac{L}{2} - x\right) - \frac{\mu_T F_{EM} L}{2}\left(\frac{L}{2} - x\right) \tag{29}$$

In Eq. (29) EI stands for the bending stiffness of the Nb$_3$Sn strand; y stands for the deflection of the buckling. After simplifying formula (29), one can get

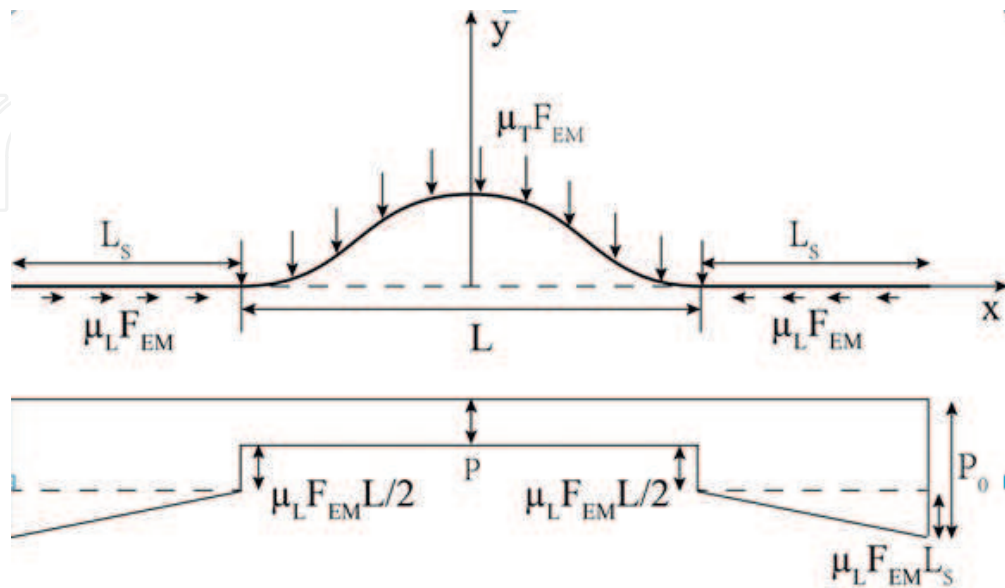$$EIy'' + Py + \frac{\mu_T F_{EM}}{2}\left(\frac{L^2}{4} - x^2\right) = 0 \tag{30}$$

Figure 8.
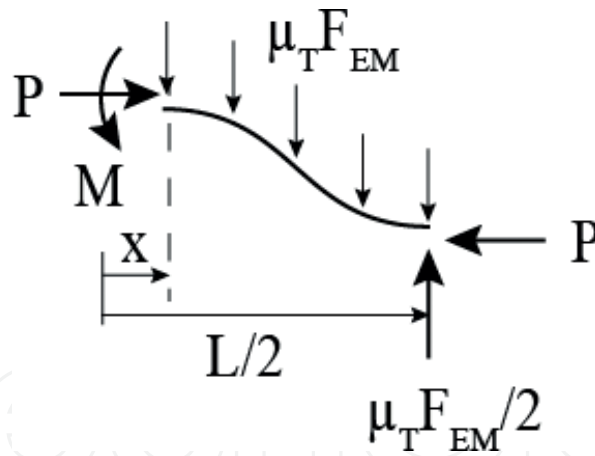*Schematic of the analytical model with the EM force.*

Figure 9.
Schematic view of the mechanical analysis for the microelement.

The general solution [27] of formula (30) is given as

$$y = \frac{m}{n^4}\left[A\cos(nx) + B\sin(nx) - \frac{n^2x^2}{2} + \frac{n^2L^2}{8} + 1\right] \qquad (31)$$

In Eq. (31), $m = \frac{\mu_T F_{EM}}{EI}$, $n^2 = \frac{P}{EI}$. Two boundary conditions are needed to solve the undetermined coefficients. After applying $y|_{x=\pm L/2} = 0$, $y'|_{x=0} = 0$ to formula (31), one can get

$$y = \frac{m}{n^4}\left[\frac{-\cos(nx)}{\cos(nL/2)} - \frac{n^2x^2}{2} + \frac{n^2L^2}{8} + 1\right] \qquad (32)$$

If we substitute the boundary $y'|_{x=\pm L/2} = 0$ to Eq. (32), Eq. (32) becomes

$$y' = \tan(nL/2) - nL/2 = 0 \qquad (33)$$

We can deduce that $nL = 8.9868...$ from Eq. (33). Therefore, the axial compression force in the buckling area is $P = 80.76EI/L^2$. There must be a balance in the axial direction between the buckling and slipping segments; we can get that

$$P_0 - P = \frac{\mu_L F_{EM} L}{2} + \mu_L F_{EM} L_S \qquad (34)$$

The geometric compatibility equation of the strand can be expressed as

$$\frac{(P_0 - P)L}{EA} - \int_{-L/2}^{L/2} \frac{1}{2}y'^2 dx + \frac{\mu_L F_{EM} L_S^2}{EA} = 0 \qquad (35)$$

Submitting Eq. (32) into Eq. (35), one can get the relation between axial force and the length of the buckling area:

$$\frac{(P_0 - P)L}{EA} - 1.597 \times 10^{-5}\left(\frac{\mu_T F_{EM}}{EI}\right)^2 L^7 + \frac{\mu_L F_{EM} L_S^2}{EA} = 0 \qquad (36)$$

Submitting Eq. (34) into Eq. (36) and eliminating the L_s, one can get

$P_0 = P + \sqrt{1.597 \times 10^{-5} EA\mu_L F_{EM} \left(\frac{\mu_T F_{EM}}{EI}\right)^2 L^7 - \frac{L^2}{4}(\mu_L F_{EM})^2}$, in which

$P = 80.76EI/L^2$.

Consider the special case $L_S = 0$ that means the end of the strand is locked and the length of the buckling is equal to the twist pitch. In this case Eq. (36) can be simplified as follows:

$$P_0 = 80.76\frac{EI}{L^2} + 1.597 \times 10^{-5} EA \left(\frac{\mu_T F_{EM}}{EI}\right)^2 L^6 \qquad (37)$$

Based on these equations, the critical buckling load P_0 can be calculated, as well as the relationship between the buckling length, bending stiffness, and the friction factor.

We can know that the strand buckling behavior is depending on the twist pitch of the first stage; the shorter the lay length, the lower the possibility of the strand buckling. The higher the wrap rigidity, the stronger the strand. Furthermore, if we fixed the coverage rate, and with a narrow wrap, which would lead to almost uniform lateral supporting, it can also prevent the strand slid into buckling. This mechanism of buckling is shown in **Figure 10**.

When there is no thermal load and EM force, the original strand in the CICCs is shown in **Figure 10(a)**. When the temperature is cooled down, the axial strain caused by thermal mismatch and the lateral compression raised by the EM load are applied to the strands. We can see that the initial "straight" strand was keeping its shape by well lateral support. When the strand working in a large magnetic field (including self-field), it bears a huge EM force. A large void is generated, at the same time, some strands bending, which is shown in **Figure 10(b)**. Additionally, this bending strain is not the only factor to make the strand fracture. For the SULTAN measurements [28], the samples is about 3.6 m long, and the high-field
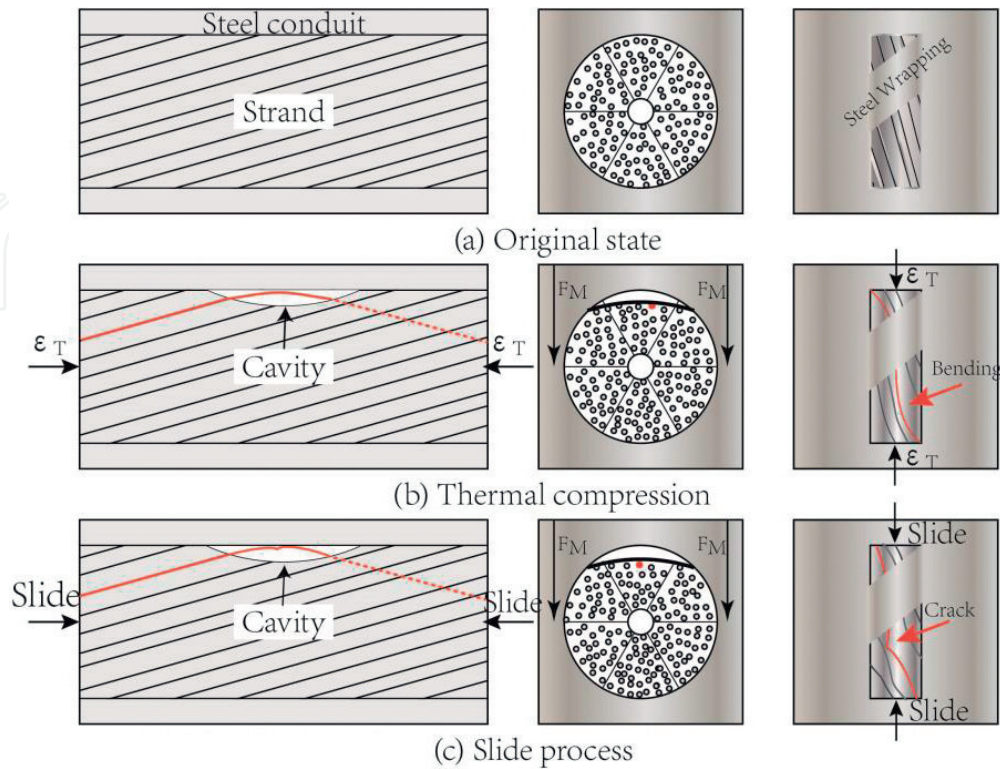

Figure 10.
Mechanism of the strand buckling behavior during the cooling and conducting processes.

region is about 0.4 m. During the EM cyclic loading, the cable can slide into the high-field region, which can accelerate the wire bending and leading the strand to fracture. This process is shown in **Figure 10(c)**.

5. Mechanical behavior of the CICC caused by electromagnetic force and thermal mismatch

The CICC qualification test samples show gradual degradation of the current-sharing temperature (Tcs) under several hundreds of EM cycles [29, 30], which leads to the Nb$_3$Sn strand's bending or compressing deformation. In this section, we focus on the relationship between Tcs and axial strain of the cable.

It is known that the ITER CS and TF coils are wounded by CICCs, which made up of five-stage sub-cables formed around a central cooling tube. The fourth petals and the sub-cables are wrapped with stainless steel tapes. Then, the wrapped cable were inserted into a stainless steel tube, which act as an amor, as illustrated in the cross-sectional view in **Figure 11**. The inner diameter of the CS armor is equal to 36 and 37 mm for TF, respectively. The side length of CS conductor is 49 mm, and the diameter of the TF conductor is of 40 mm. More than 1000 Nb3Sn strands were in the CICC conductors. In this section, the conductors can be simplified into a rope and the petals with circle cross section, as shown in **Figure 11**. Thus, the cable could be analyzed by using the thin rod model as shown in **Figure 12**.

During the calculations, the parameters R, R$_{in}$, and twist pitch (h) are 6, 6, and 450 mm, respectively. According to the geometric relation $h = 2\pi r \tan \alpha$, as shown in **Figure 13(b)**, we can get $\alpha = 80.5°$, where α represents the initial helix angle. **Figure 13(a)** also displays the loads acting on the petal and the geometric relation of the petal centerline.
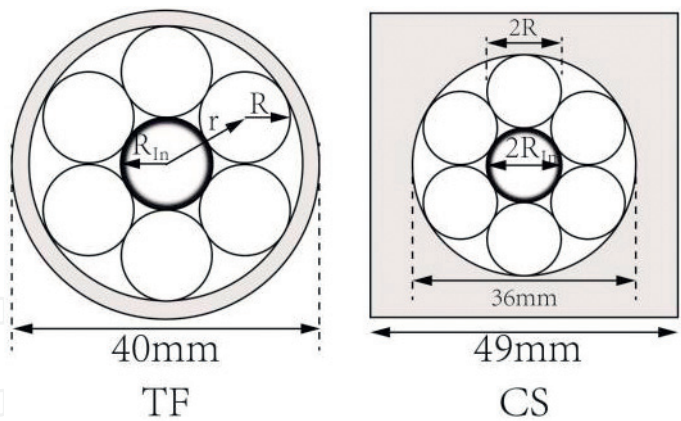

Figure 11.
Schematic illustration of the CS and TF CICC cross sections. The symbols R$_{in}$ and R denote the radius of the He channel and petal, respectively; r is on behalf of the sum of R$_{in}$ and R: r = R$_{In}$ + R.
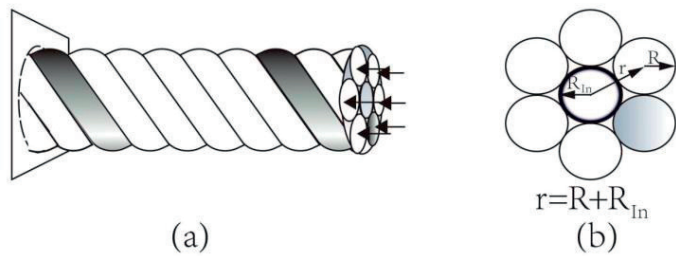

Figure 12.
(a) The deformation of the cable caused by the axial compression; (b) the cross section of the cable.
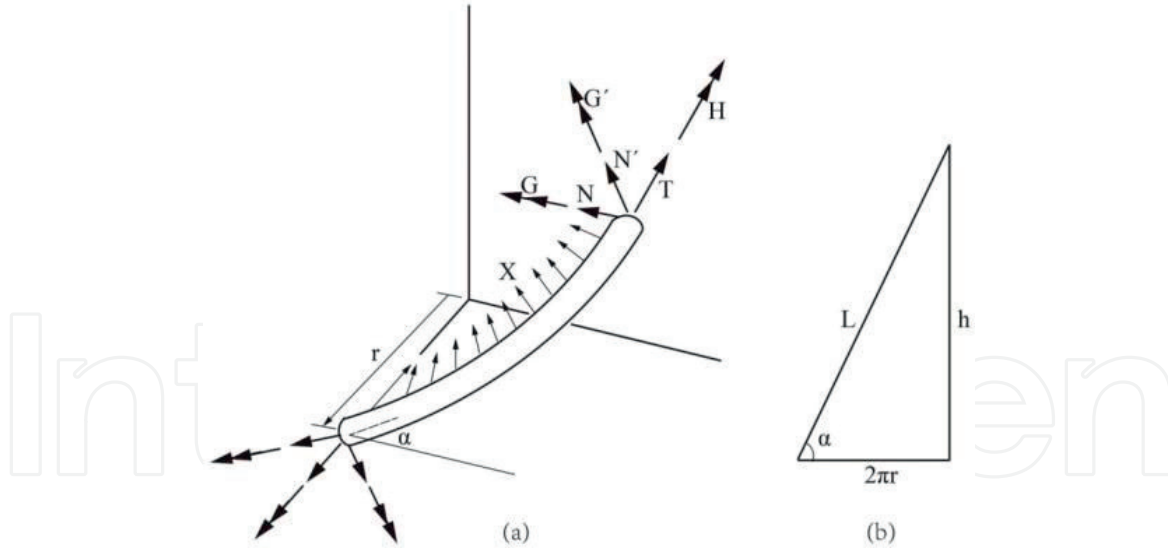
Figure 13.
(a) Uniform forces acting on the petal; (b) geometric relation of the petal centerline.

Assume that the petals were contact with each other in the original state. The curvature and the twist per unit length of the petal is *k, k', τ*; then the changes can be written as Δ*k*, Δ*k'*, Δ*τ*. They can be expressed as [19]

$$\Delta\kappa' = \frac{\cos^2\bar{\alpha}}{\bar{r}} - \frac{\cos^2\alpha}{r} = \frac{-\cos^2\alpha}{r}\frac{\Delta r}{r} - 2\frac{\sin\alpha\cos\alpha}{r}\Delta\alpha \tag{38}$$

$$\Delta\tau = \frac{\cos\bar{\alpha}\sin\bar{\alpha}}{\bar{r}} - \frac{\cos\alpha\sin\alpha}{r} = \frac{-\sin\alpha\cos\alpha}{r}\frac{\Delta r}{r} + \frac{(1 - 2\sin^2\alpha)}{r}\Delta\alpha \tag{39}$$

In Eqs. (38) and (39), α and $\bar{\alpha}$ is the initial and final helical angle of the petal, $\Delta\alpha$ and Δr stand for the change of helical angle and radius of the petal, and r and $\bar{r}$ denote the original and final radius, respectively. The loads and moments can be deduced as.

$$G' = \frac{E\pi R^4}{4}\Delta\kappa'; H = \frac{E\pi R^4}{4(1+\nu)}\Delta\tau; T = \pi ER^2\xi \tag{40}$$

Here, T, G', H stand for the axial load, bending moment, and twist moment of the petal, respectively; E is of the axial stiffness of the petal, v is Poisson's ratio, and ξ stands for the strain in the axial direction of the petal. If the petal is free in the initial state and there is no contact force under the compression state, then the uniform load between the petals is equal to zero. According to the thin rod model presented by Costello [19], the following equation is satisfied:

$$X = N'\frac{\sin\alpha\cos\alpha}{r} - T\frac{\cos^2\alpha}{r} = 0 \tag{41}$$

$$N' = H\frac{\cos^2\alpha}{r} - G'\frac{\sin\alpha\cos\alpha}{r} \tag{42}$$

In Eqs. (41) and (42), X stands for the resultant contact force per unit length of a petal; N' is of the shear force acting on the petal. From Eqs. (38)–(40) and Eq. (42), the shearing force N' acting on the petal can be written as

$$\frac{N'}{ER^2} = \frac{\pi v\sin\alpha\cos^3\alpha}{4(r/R)^2(1+v)}\frac{\Delta r}{r} + \frac{\pi\cos^2\alpha}{4(r/R)^2}\left(\frac{1 - 2\sin^2\alpha}{1+v} + 2\sin^2\alpha\right)\Delta\alpha \tag{43}$$

Substituting Eqs. (40) and (43) into Eq. (41), the axial strain of the petal ξ which is only related to the Δr and $\Delta \alpha$ can be written as

$$\xi = \frac{v \sin^2\alpha \cos^2\alpha}{4(r/R)^2(1+v)} \frac{\Delta r}{r} + \frac{\sin\alpha \cos\alpha}{4(r/R)^2} \left(\frac{1 - 2\sin^2\alpha}{1+v} + 2\sin^2\alpha \right) \Delta\alpha \qquad (44)$$

The deformed configuration of the petal in **Figure 13** yields

$$\varepsilon = \frac{\overline{h} - h}{h} = \xi + \frac{\Delta\alpha}{\tan\alpha} \qquad (45)$$

From Eqs. (44) and (45), one can get

$$\varepsilon = \frac{v \sin^2\alpha \cos^2\alpha}{4(r/R)^2(1+v)} \frac{\Delta r}{r} + \left[\frac{\cos\alpha}{\sin\alpha} + \frac{\sin\alpha \cos\alpha}{4(r/R)^2} \left(\frac{1 - 2\sin^2\alpha}{1+v} + 2\sin^2\alpha \right) \right] \Delta\alpha \quad (46)$$

The angle of twist per unit length τ of the petal can be defined by the expression

$$r\tau_c = r\frac{\overline{\theta} - \theta}{h} = \frac{r}{\overline{r}} \left(\frac{1 + \xi}{\tan\alpha} - \Delta\alpha \right) - \frac{1}{\tan\alpha} \qquad (47)$$

That is,

$$r\tau_c = \left[\frac{v \sin\alpha \cos^2\alpha}{4(r/R)^2(1+v)} - \frac{\cos\alpha}{\sin\alpha} \right] \frac{\Delta r}{r} + \left[\frac{\cos^2\alpha}{4(r/R)^2} \left(\frac{1 - 2\sin^2\alpha}{1+v} + 2\sin^2\alpha \right) - 1 \right] \Delta\alpha$$

$$(48)$$

At the two ends of the petal per twist pitch, the rotation is zero, and the compression strain obeys: $\varepsilon = -\varepsilon_0$; then, Eq. (46) and Eq. (48) become

$$\begin{cases} -\varepsilon_0 = \dfrac{v \sin^2\alpha \cos^2\alpha}{4(r/R)^2(1+v)} \dfrac{\Delta r}{r} + \left[\dfrac{\cos\alpha}{\sin\alpha} + \dfrac{\sin\alpha \cos\alpha}{4(r/R)^2} \left(\dfrac{1 - 2\sin^2\alpha}{1+v} + 2\sin^2\alpha \right) \right] \Delta\alpha \\[3mm] 0 = \left[\dfrac{v \sin\alpha \cos^2\alpha}{4(r/R)^2(1+v)} - \dfrac{\cos\alpha}{\sin\alpha} \right] \dfrac{\Delta r}{r} + \left[\dfrac{\cos^2\alpha}{4(r/R)^2} \left(\dfrac{1 - 2\sin^2\alpha}{1+v} + 2\sin^2\alpha \right) - 1 \right] \Delta\alpha \end{cases}$$

$$(49)$$

The relation between axial strain ε_0 and transverse strain $\varepsilon_{Trans} = \frac{\Delta r}{r}$ can be expressed as

$$\varepsilon_{Trans} = \frac{C_4}{C_2 C_3 - C_1 C_4} \varepsilon_0 \qquad (50)$$

where $C_1 = \frac{v \sin^2\alpha \cos^2\alpha}{4(r/R)^2(1+v)}$, $C_2 = \frac{\cos\alpha}{\sin\alpha} + \frac{\sin\alpha \cos\alpha}{4(r/R)^2} \left(\frac{1 - 2\sin^2\alpha}{1+v} + 2\sin^2\alpha \right)$,

$C_3 = \frac{v \sin\alpha \cos^2\alpha}{4(r/R)^2(1+v)} - \frac{\cos\alpha}{\sin\alpha}$, $C_4 = \frac{\cos^2\alpha}{4(r/R)^2} \left(\frac{1 - 2\sin^2\alpha}{1+v} + 2\sin^2\alpha \right) - 1$.

It is found that the coefficient between transverse and axial strains is affected by the helical angle α and Poisson's ratio v. When the twist pitch of the fifth stage cable is of 427, 450, and 476 mm, the corresponding helical angle of the petal equals to 80, 80.5, and 81°, respectively. Substituting these values into Eq. (50), one can see that the axial strain of the cable ε_0 has a linear relationship with the transverse strain ε_{Trans}, which is displayed in **Figure 14**. We carried out an experiment by
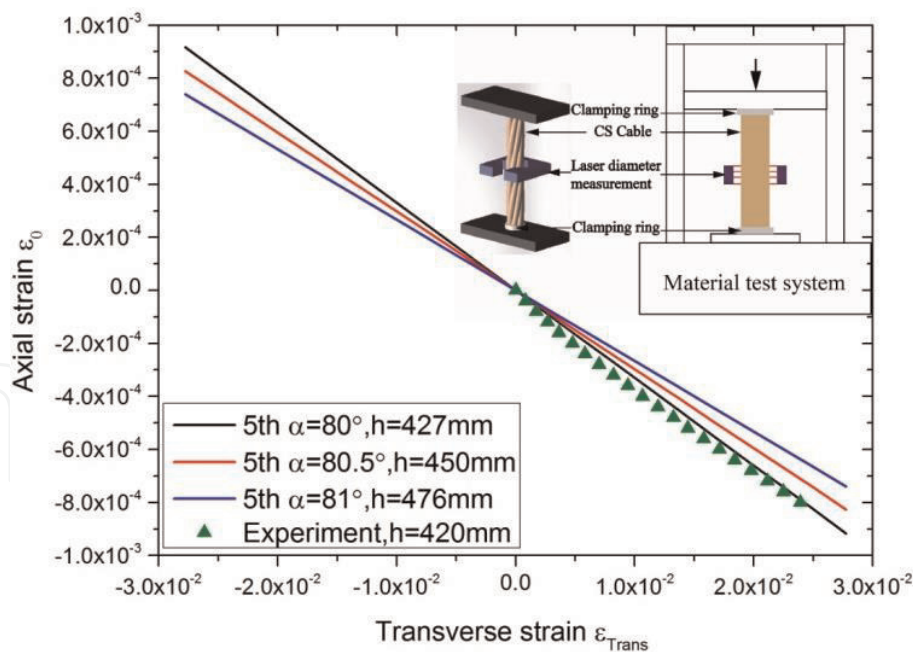
Figure 14.
Relationship between the axial strain ε_0 and the transverse strain ε_T. The colored lines are obtained by using the presented theoretical model. The green triangle symbols denote the experimental results.

compressing a CS cable which was fabricated in CASIPP to validate the analytical model. When the CS cable specimen is compressed along axial direction, it extends transversely with high resolution. The transverse extension can be measured by using a laser sensor. The experimental setup is schematically illustrated in the inset of **Figure 14**. One can find that the theoretical model shows perfect consistency with the experiment.

In **Figure 14**, we can get that the CS conductors with baseline and LTP (long twist pitch) shows a Tcs degradation after EM cycles, while for the samples with
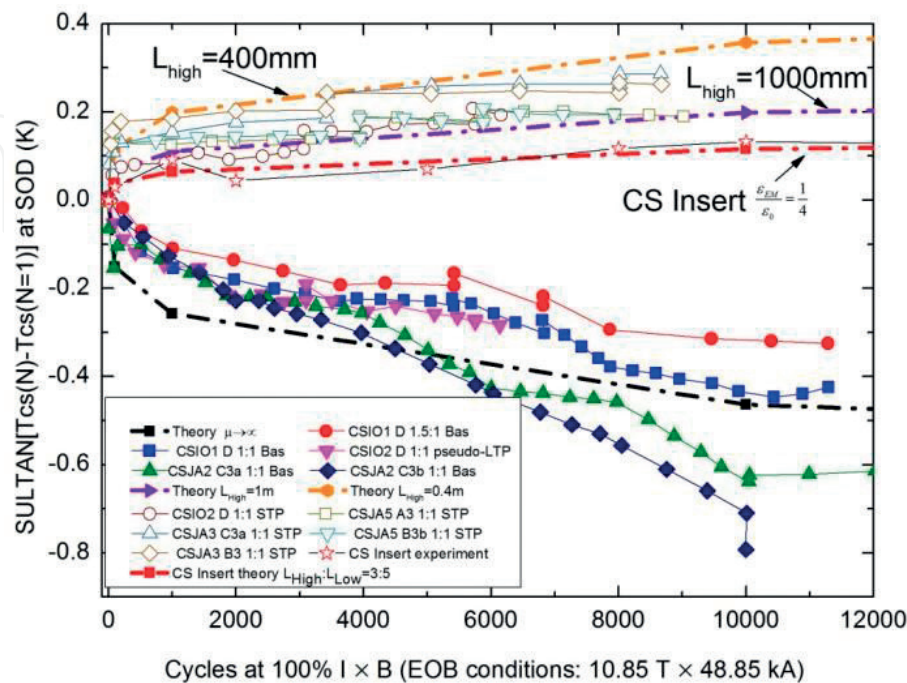

Figure 15.
A comparison of the experimental results and theoretical results based on the presented model [18].

STP (short twist pitch) shows an opposite phenomenon, the Tcs becomes a constant even have an enhanced. These experimental results presented in Ref. [30] have a contrast with analytical prediction for many years. Using the theoretical model proposed in this chapter, the Tcs enhancement and degradation behaviors can be predicted quantitatively. **Figure 15** shows a comparison of calculated results and experimental results, where the lines show the theoretical results and the dots are the experimental results. It is found that during the primary stage of the EM cycle there was a quick increase of axial strain that will lead to the Tcs drop dramatically. With the same reason, samples with LTP and baseline show an obviously degradation; this same rule applies to TF conductors. However, several STP CS conductors have an increase of Tcs, which means that the initial axial compression strain has been released by the EM loads, squeezing the cables at the high-field zone into the low-field region.

While it is easy to imagine when the expansions of the cable in the high-field zone get stacked, the strain will not be released and the Tcs will drop (see the black dash line in **Figure 15**). If the inner part of the conductor is smooth enough, the axial compression strain is released completely, the Tcs reaches its upper boundary which is shown by the orange dash line with circle symbol corresponding to the length of the high-field region is 400 mm. If the high-field region's length is 1000 mm, then the lower boundary of the enhancing Tcs is given with purple line with triangle symbol. We can find that the theoretical results agree with the experimental results very well.

6. Discussion

In the past half-century, the structure of CICC conductor was under continuous optimization and improvement. The CICC conductors have so many advantages such as good self-support, high operational stability, high current carrying capacity, low AC loss, etc., and they are widely used in the superconducting magnets. The nuclear fusion device CFTER built by China has also chosen the CICC conductors. However, there still have some problems to be solved: (1) there is a necessity for theoretical model to explain the degradation of critical current caused by mechanical deformation for the Nb3Sn strand; (2) accurate description of the mechanical response of complex strand structures in the coupling fields remains a challenging problem; (3) the untwisting behavior during the cable penetration is still not suppressed completely. One needs a more effective model to optimize the manufacturing process; and (4) the long-term stability and real-time monitoring of superconducting magnets are also a challenge for the engineers. Based on this, the equivalent mechanical parameters of CICC conductors and their mechanical behavior under coupled fields will be further studied. The authors hope that these models can provide a valuable reference for the related researchers.

Acknowledgements

Author details

Donghua Yue[1,2,3], Xingyi Zhang[1,2]* and Youhe Zhou[1,2]

1 Department of Mechanics and Engineering Sciences, College of Civil Engineering and Mechanics, Lanzhou University, Lanzhou, China

2 Key Laboratory of Mechanics on Disaster and Environment in Western China Attached to the Ministry of Education of China, Lanzhou University, Lanzhou, P.R. China

3 Institute of Systems Engineering, China Academy of Engineering Physics, Mianyang, China

*Address all correspondence to: zhangxingyi@lzu.edu.cn

IntechOpen

References

[1] Motojima O. The ITER project construction status. Nuclear Fusion. 2015;**55**(10):104023

[2] Mitchell N, Bessette D, Gallix R, et al. The ITER magnet system. IEEE Transactions on Applied Superconductivity. 2008;**18**(2):435-440

[3] File J, Martin GD, Mills RG, et al. Stabilized, levitated superconducting rings. Journal of Applied Physics. 1968;**39**(6):2623-2626

[4] Hoenig MO. Internally cooled cabled superconductors. Cryogenics. 1980;**20**(7):373-389

[5] Lubell MS, Chandrasekhar BS, Mallick GT. Degradation and flux jumping in solenoids of heat-treated Nb-25% Zr wire. Applied Physics Letters. 1963;**3**(5):79-80

[6] Hoenig M, Montgomery D. Dense supercritical-helium cooled superconductors for large high field stabilized magnets. IEEE Transactions on Magnetics. 1975;**11**(2):569-572

[7] Lue J. Review of stability experiments on cable-in-conduit conductors. Cryogenics. 1994;**34**(10): 779-786

[8] Ekin J. Strain scaling law for flux pinning in practical superconductors. Part 1: Basic relationship and application to Nb3Sn conductors. Cryogenics. 1980; **20**(11):611-624

[9] Nijhuis A. A solution for transverse load degradation in ITER Nb3Sn CICCs: Verification of cabling effect on Lorentz force response. Superconductor Science and Technology. 2008;**21**(5):054011

[10] Zhu JY, Luo W, Zhou YH, et al. Contact mechanical characteristics of Nb3Sn strands under transverse electromagnetic loads in the CICC cross-section. Superconductor Science and Technology. 2012;**25**(12):125011

[11] Feng J. A cable twisting model and its application in CSIC multi-stage cabling structure. Fusion Engineering and Design. 2009;**84**(12):2084-2092

[12] Qin J, Wu Y, Warnet LL, et al. A novel numerical mechanical model for the stress–strain distribution in superconducting cable-in-conduit conductors. Superconductor Science and Technology. 2011;**24**(6):065012

[13] Qin J-G, Xue T-J, Liu B, et al. Cabling Technology of Nb3Sn conductor for CFETR central solenoid model coil. IEEE Transactions on Applied Superconductivity. 2016; **26**(3):1-5

[14] Qin J, Dai C, Liu B, et al. Optimization of CFETR CSMC cabling based on numerical modeling and experiments. Superconductor Science & Technology. 2015;**28**(12):125008

[15] Yue D, Zhang X, Yong H, Zhou J, Zhou YH. Controllable rectification of the axial expansion in the thermally driven artificial muscle. Applied Physics Letters. 2015;**107**(11):111903

[16] Donghua Y, Xingyi Z, Youhe Z. Buckling behavior of Nb3Sn strand caused by electromagnetic force and thermal mismatch in ITER cable-in-conduit conductor. IEEE Transactions on Applied Superconductivity. 2017; **27**(7):1

[17] Qin J, Yee D, Zhang X, Wu Y, Liu X, Liu H, et al. Rotation analysis on large complex superconducting cables based on numerical modeling and experiments. Superconductor Science and Technology. 2018;**31**(2):025001

[18] Yue D, Zhang X, Zhou Y-H. Theoretical analysis for the mechanical behavior caused by an electromagnetic cycle in ITER Nb3Sn cable-in-conduit conductors. Acta Mechanica Sinica. 2018;**34**(4):614-622

[19] Costello GA. Theory of Wire Rope. New York: Springer Science & Business Media; 1997

[20] Nabara Y, Suwa T, Takahashi Y, et al. Behavior of cable assembled with conduit for ITER central solenoid. IEEE Transactions on Applied Superconductivity. 2015;**25**(3):1-5

[21] Hetenyi M. Beams on Elastic Foundation: Theory with Applications in the Fields of Civil and Mechanical Engineering. 1971

[22] Niu K. Compressive Behavior of Sandwich Panels and Laminates with Damage, Georgia Institute of Technology, Atlanta. 1998

[23] Niu K, Talreja R. Buckling of a thin face layer on Winkler foundation with debonds. Journal of Sandwich Structures and Materials. 1999;**1**(4): 259-278

[24] Mitchell N, Devred A, Larbalestier DC, et al. Reversible and irreversible mechanical effects in real cable-in-conduit conductors. Superconductor Science and Technology. 2013;**26**(11): 114004

[25] Li Y, Ta W, Gao Y. Prediction for IC degradation of superconducting strand under bending. Cryogenics. 2013;**58**: 20-25

[26] Li Y, Yang T, Zhou Y, et al. Spring model for mechanical–electrical properties of CICC in cryogenic–electromagnetic environments. Cryogenics. 2014;**62**:14-30

[27] Hobbs RE. Pipeline buckling caused by axial loads. Journal of Constructional Steel Research. 1981;**1**(2):2-10

[28] March SA, Bruzzone P, Stepanov B, et al. Results of the TFEU6 sample tested in SULTAN. IEEE Transactions on Applied Superconductivity. 2013; **23**(3):4200204

[29] Martovetsky NN, Reiersen WT, Murdoch GR, Bruzzone P, Stepanov B. Qualification of the US conductors for ITER TF magnet system. ITPS. 2018; **46**(5):1477-1483

[30] Devred A, Backbier I, Bessette D, et al. Challenges and status of ITER conductor production. Superconductor Science and Technology. 2014;**27**(4): 044001